DØnote 4760-CONF

Search for the Higgs boson in $H \to WW^{(*)} \to \ell^+\nu\,\ell'^-\bar{\nu}$ $(\ell, \ell' = e, \mu)$ decays in $p\bar{p}$ collisions at $\sqrt{s} = 1.96$ TeV

The DØ Collaboration
URL http://www-d0.fnal.gov
(Dated: March 14, 2005)

We present a search for the standard model Higgs boson in $H \to WW^{(*)} \to \ell^+\nu\,\ell'^-\bar{\nu}$ $(\ell, \ell' = e, \mu)$ decays in $p\bar{p}$ collisions at a center-of-mass energy of $\sqrt{s} = 1.96$ TeV. The data, collected from April 2002 to June 2004 with the Run II DØ detector, correspond to an integrated luminosity of 325 pb^{-1} in the e^+e^-, 318 pb^{-1} in the $e^\pm\mu^\mp$ and 299 pb^{-1} in the $\mu^+\mu^-$ final state. The number of events observed is consistent with expectations from standard model backgrounds. Limits from the combination of all three channels on the production cross section times branching ratio $\sigma \times BR(H \to WW^{(*)})$ are presented.

Preliminary Results for Winter 2005 Conferences

In the standard model (SM) the Higgs boson is crucial to the understanding of electroweak symmetry breaking and the mass generation of electroweak gauge bosons and fermions. Direct searches at the CERN e^+e^- collider (LEP) yield a lower limit for the Higgs boson mass of $m_H > 114.4\,\text{GeV}$ [1] at 95% confidence level (C.L). Indirect measurements via fits to the electroweak precision data give an upper bound of $m_H < 251\,\text{GeV}$ [2] at 95% confidence level. The next-to-leading order (NLO) calculations [3, 4] for the production cross section times the branching ratio $\sigma \times BR(H \to WW^{(*)})$ predict a cross section of 2.69 fb for a standard model Higgs boson mass of m_H= 160 GeV.

In this conference note we present a search for the Higgs boson in $H \to WW^{(*)} \to \ell^+\nu\,\ell'^-\bar{\nu}$ $(\ell, \ell' = e, \mu)$ decays. We use data collected between April 2002 and June 2004 in $p\bar{p}$ collisions at $\sqrt{s} = 1.96$ TeV of Run II of the Tevatron Collider. The integrated luminosities are 325 ± 21 pb^{-1}, 318 ± 21 pb^{-1}, and 299 ± 19 pb^{-1} for the e^+e^-, $e^\pm\mu^\mp$, and $\mu^+\mu^-$ channels, respectively. The differences in the integrated luminosities for various channels are primarily due to different trigger conditions.

We briefly describe the main components of the DØ Run II detector [5] important to this analysis. The central tracking system consists of a silicon microstrip tracker (SMT) and a central fiber tracker (CFT), both located within a 2.0 T axial magnetic field. The SMT strips have a typical pitch of 50–80 μm, and the design is optimized for tracking and vertexing over the pseudorapidity range $|\eta| < 3$, where $\eta = -\ln(\tan\frac{\theta}{2})$ with polar angle θ. The system has a six-barrel longitudinal structure, each with a set of four silicon layers arranged axially around the beam pipe, interspersed with sixteen radial disks. The CFT has eight thin coaxial barrels, each supporting two doublets of overlapping scintillating fibers of 0.835 mm diameter, one doublet parallel to the beam axis, the other alternating by $\pm 3^\circ$ relative to the beam axis.

A liquid-argon/uranium calorimeter surrounds the central tracking system and consists of a central calorimeter (CC) covering to $|\eta| \approx 1.1$, and two end cap calorimeters (EC) extending coverage for $|\eta| < 4.2$, all housed in separate cryostats [6]. Scintillators between the CC and EC cryostats provide sampling of showers for $1.1 < |\eta| < 1.4$.

The muon system is located outside the calorimeters and consists of a layer of tracking detectors and scintillation trigger counters inside toroid magnets which provide a 1.8 T magnetic field, followed by two similar layers behind each toroid. Tracking in the muon system for $|\eta| < 1$ relies on 10 cm wide drift tubes [6], while 1 cm mini-drift tubes are used for $1 < |\eta| < 2$ [7].

The $H \to WW^{(*)} \to \ell^+\nu\,\ell'^-\bar{\nu}$ candidates are selected by triggering on single or di-lepton events using a three level trigger system. The first trigger level uses hardware to select electron candidates based on energy deposition in the electromagnetic part of the calorimeter and selects muon candidates formed by hits in two layers of the muon scintillator system. Digital signal processors in the second trigger level form muon track candidate segments defined by hits in the muon drift chambers and scintillators. At the third level, software algorithms running on a computing farm and exploiting the full event information are used to make the final selection of events which are recorded for offline analysis.

In the further offline analysis electrons are identified by electromagnetic showers in the calorimeter. These showers are chosen by comparing the longitudinal and transverse shower profiles to those of simulated electrons. The showers must be isolated, deposit most of their energy in the electromagnetic part of the calorimeter, and pass a likelihood criterion that includes a spatial track match and, in the CC region, an E/p requirement, where E is the energy of the calorimeter cluster and p is the momentum of the track. All electrons are required to be in the pseudorapidity range $|\eta| < 3.0$. The transverse momentum measurement of the electrons is based on calorimeter cell energy information.

Muon tracks are reconstructed from hits in the wire chambers and scintillators in the muon system and must match a track in the central tracker. To select isolated muons, the scalar sum of the transverse momentum of all tracks other than that of the muon in a cone of $\mathcal{R} = 0.5$ around the muon track must be less than 4 GeV, where $\mathcal{R} = \sqrt{(\Delta\phi)^2 + (\Delta\eta)^2}$ and ϕ is the azimuthal angle. Muon detection is restricted to the coverage of the muon system $|\eta| < 2.0$. Muons from cosmic rays are rejected by requiring a timing criterion on the hits in the scintillator layers as well as applying restrictions on the position of the muon track with respect to the primary vertex.

The decay of two W bosons into electrons or muons results in three different final states $e^+e^- + X$ (ee channel), $e^\pm\mu^\mp + X$ ($e\mu$ channel), and $\mu^+\mu^- + X$ ($\mu\mu$ channel), each of which consists of two oppositely charged isolated high transverse momentum, p_T, leptons and large missing transverse energy, $\not\!\!E_T$, due to the escaping neutrinos. The selection criteria for each channel were chosen to maximize the expected limit, while keeping high efficiency for $H \to WW^{(*)}$ production. To exploit the full kinematic range that changes with increasing Higgs mass various cuts are used dependent on the Higgs boson mass m_H. Six Higgs boson masses $m_H$from 100 GeV to 200 GeV have been chosen.

In all three channels, two leptons originating from the same vertex are required to be of opposite charge, and must have $p_T > 15$ GeV for the leading lepton and $p_T > 10$ GeV for the trailing one (Cut 1). Figure 1 shows the good agreement between data and Monte Carlo (MC) in $\Delta\phi_{\ell\ell}$ distributions for the ee channel (a), the $\mu\mu$ channel (c) and the $e\mu$ channel (e) after applying the lepton transverse momentum cuts. In Fig. 2 the distributions for the leading and trailing lepton, the missing transverse energy and the invariant di-lepton mass are shown for the ee channel while Fig. 3 shows identical distributions for the $e\mu$ final state. Fig. 4 shows the distribution of the scaled missing transverse

TABLE I: Selection efficiency (in %) for $H \to WW^{(*)}$ decays for the three channel after all cuts. Quoted are the overall errors, combining statistical and systematic uncertainties in quadrature.

m_H (GeV)	ee	$e\mu$	$\mu\mu$
100	3.9 ± 0.3	4.1 ± 0.3	4.0 ± 0.4
120	8.0 ± 0.6	8.5 ± 0.5	8.4 ± 0.4
140	10.3 ± 0.5	11.9 ± 0.6	10.6 ± 0.5
160	13.6 ± 0.6	16.6 ± 0.8	15.2 ± 0.6
180	13.0 ± 0.7	16.7 ± 0.8	12.5 ± 0.6
200	10.3 ± 0.5	14.2 ± 0.6	11.6 ± 0.5

energy $\not\!\!E_T^{\rm Sc}$ (defined later in the text) and the sum of the leading and trailing muon transverse momentum p_T and the missing transverse energy $\not\!\!E_T$ after applying the initial transverse momentum cuts in the $\mu\mu$ channel.

In all cases, the background is largely dominated by Z/γ^* production which is suppressed by requiring the missing transverse energy $\not\!\!E_T$ to be greater than 20 GeV in all three channels (Cut 2). Events are also removed if the $\not\!\!E_T$ has a large contribution from the mis-measurement of jet energy, using the following procedure. The fluctuation in the measurement of jet energy in the transverse plane can be approximated by $\Delta E^{\rm jet} \cdot \sin\theta^{\rm jet}$ where $\Delta E^{\rm jet}$ is proportional to $\sqrt{E^{\rm jet}}$. The opening angle $\Delta\phi\,({\rm jet}, \not\!\!E_T)$ between this projected energy fluctuation and the missing transverse energy provides a measure of the contribution of the jet to the missing transverse energy. The scaled missing transverse energy is defined as

$$\not\!\!E_T^{\rm Sc} = \frac{\not\!\!E_T}{\sqrt{\sum_{\rm jets} \left(\Delta E^{\rm jet} \cdot \sin\theta^{\rm jet} \cdot \cos\Delta\phi\,({\rm jet}, \not\!\!E_T)\right)^2}}\ . \tag{1}$$

It is required to be greater than 15 (Cut 3). As discussed below, the charged lepton system and the neutrinos are emitted back–to–back, the invariant mass for the Higgs decays is restricted to $m_H/2$. Thus, depending on the Higgs boson mass m_H the invariant mass $m_{\ell\ell}$ is required to be $m_{\ell\ell} < m_H/2\,{\rm GeV}$ (Cut 4). In the $\mu\mu$ channel a lower cut boundary with $m_{\ell\ell} > 20\,{\rm GeV}$ is required to remove events from J/ψ and Υ production. The sum of the lepton transverse momentum p_T and the missing transverse momentum $\not\!\!E_T$ is required to be in the range $m_H/2 + 20\,{\rm GeV} < p_T^{\ell_1} + p_T^{\ell_2} + \not\!\!E_T < m_H$ for the ee and $e\mu$ channel and $m_H/2 + 10\,{\rm GeV} < p_T^{\ell_1} + p_T^{\ell_2} + \not\!\!E_T < m_H$ for the $\mu\mu$ channel (Cut 5). The transverse mass $m_T^{\ell\ell} = \sqrt{2 p_T^{\ell\ell} \not\!\!E_T (1 - \cos\Delta\phi(\ell\ell, \not\!\!E_T))}$ computed from the di–lepton momentum and the missing transverse momentum should be in the range $m_H/2 < m_T < m_H - 10\,{\rm GeV}$ (Cut 6). The latter two cuts further reduce backgrounds from Z/γ^* production. Finally, to suppress the background from $t\bar{t}$ production, the scalar sum of the transverse energies of all jets with $E_T^{\rm jet} > 20$ GeV and $|\eta| < 2.5$, H_T, is required to be less than 100 GeV (Cut 7). Remaining Z boson and multi-jet events can be rejected with a cut on the opening angle $\Delta\phi_{\ell\ell}$, since most of the background decays are back-to-back. This is not the case for Higgs boson decays because of the spin correlations in the decay. The cut is applied at $\Delta\phi_{\ell\ell} < 2.0$ (Cut 8).

To give the best exclusion limits the selection in the $\mu\mu$ channel is slightly changed for Higgs boson masses m_H= 140 and 160 GeV. For a better Z/γ^* background suppression cuts 4, 5 and 6 are exchanged by the following cuts: The invariant mass $m_{\mu\mu}$ should be in the range $20\,{\rm GeV} < m_{\mu\mu} < 80\,{\rm GeV}$ (Cut 4). Since the momentum resolution is degraded for high p_T tracks, an additional constrained fit is performed to reject events compatible with Z boson production (Cut 5). The sum of the muon transverse momenta and the missing transverse energy should be $p_{\rm T}^{\mu 1} + p_{\rm T}^{\mu 2} + \not\!\!E_T > 90\,{\rm GeV}$ (Cut 6).

The efficiency for $H \to WW^{(*)}$ signal events to pass the acceptance and kinematic criteria is determined using the PYTHIA 6.2 [8] event generator followed by a detailed GEANT-based [9] simulation of the DØ detector. All trigger and reconstruction efficiencies are derived from the data. The overall detection efficiency ranges from $(3.9 \pm 0.2)\%$ to $(16.7 \pm 0.8)\%$ depending on the decay channel and the m_H dependent selection. Table I summarizes all these numbers.

The efficiency for $H \to WW^{(*)}$ signal events to pass the acceptance and kinematic criteria is determined using the PYTHIA 6.2 [8] event generator followed by a detailed GEANT-based [9] simulation of the DØ detector. All trigger and reconstruction efficiencies are derived from the data. The overall detection efficiency ranges from $(3.9 \pm 0.2)\%$ to $(16.7 \pm 0.8)\%$ depending on the decay channel and the m_H dependent selection. Table I summarizes all these numbers.

Using the NLO cross sections calculated with HIGLU [4] and HDECAY [3] and branching fractions B of 0.1068 ± 0.0012 for $W \to l\nu$ [10], the expected number of events for $H \to WW^{(*)}$ decays combined for all three channels is $0.54 \pm 0.02({\rm stat}) \pm 0.05({\rm syst}) \pm 0.04({\rm lum})$ events for a Higgs boson mass m_H= 160 GeV, where the statistical error is given by the statistics of the MC sample. The signal breakdown for the combination of the three channels is given in the first line of Table II.

TABLE II: Number of signal and background events expected and number of events observed after all selections are applied for the combination of all three channels. Only statistical uncertainties are given.

m_H(GeV)	100	120	140	160	180	200
$H \to WW^{(*)}$	0.007 ± 0.001	0.11 ± 0.01	0.33 ± 0.01	0.54 ± 0.02	0.36 ± 0.01	0.17 ± 0.01
Z/γ^*	8.2 ± 1.1	8.2 ± 1.1	3.4 ± 0.7	3.3 ± 0.7	6.6 ± 0.9	9.4 ± 1.1
Diboson	4.7 ± 0.1	7.4 ± 0.1	10.9 ± 0.2	11.7 ± 0.2	10.9 ± 0.2	9.5 ± 0.2
$t\bar{t}$	0.04 ± 0.01	0.12 ± 0.02	0.30 ± 0.02	0.44 ± 0.03	0.65 ± 0.05	0.77 ± 0.05
W+jet/γ	17.6 ± 2.6	14.3 ± 2.2	6.6 ± 1.5	2.1 ± 0.7	0.6 ± 0.4	0.0 ± 0.0
Multijet	0.6 ± 0.3	0.3 ± 0.1	0.2 ± 0.1	0.2 ± 0.1	0.3 ± 0.1	0.3 ± 0.1
Background sum	31.0 ± 2.8	30.2 ± 2.5	21.4 ± 1.6	17.7 ± 1.0	19.1 ± 1.0	20.0 ± 1.1
Data	25	23	21	20	20	16

TABLE III: Summary of the systematic uncertainties in percent for ee, $e\mu$, and $\mu\mu$ channels on the uncertainty of the $H \to WW^{(*)}$ signal efficiency and the number of background events (BG) excluding the uncertainty on the luminosity measurement.

	ee		$e\mu$		$\mu\mu$	
m_H	Signal	BG	Signal	BG	Signal	BG
(GeV)	Uncertainty in %					
100	6.5	9.5	4.0	11.4	5.0	7.2
120	6.4	8.6	4.4	13.6	4.1	7.5
140	3.8	6.7	4.8	13.6	4.0	8.3
160	4.1	7.3	4.5	12.0	3.8	8.3
180	4.5	10.3	4.3	13.0	4.2	14.6
200	4.4	10.6	3.5	12.3	3.4	18.1

Background contributions from Z/γ^*, W+jet/γ, $t\bar{t}$, WW, WZ and ZZ events are estimated using the PYTHIA event generator. In addition, W+jet/γ contributions are verified using ALPGEN [11]. All events are processed through the full detector simulation. The background due to multijet production, when a jet is misidentified as an electron, is determined from the data using a sample of like-sign di-lepton events with inverted lepton quality cuts (called QCD background in Fig. 1).

For the normalization of Z/γ^* and W+jet/γ events, the NNLO cross sections from Ref. [12] are used. The cross section times branching ratio of Z/γ^* production in the invariant mass region $60\,\text{GeV} < m_{\ell\ell} < 130\,\text{GeV}$ is $\sigma \times BR = 254$ pb. For inclusive W boson production with decays into a single lepton flavor state, this value is $\sigma \times BR = 2717$ pb. The NLO WW, WZ and ZZ production cross section values are taken from Ref. [13] with $\sigma \times BR = 0.15$ pb for WW, $\sigma \times BR = 0.014$ pb for WZ and $\sigma \times BR = 0.002$ pb for ZZ production with decay into a single lepton flavor state. The calculations of Ref. [14] are used for $t\bar{t}$ production with $\sigma \times BR = 0.076$ pb with single flavor lepton decays of both W bosons. A summary of the background contributions together with signal expectations and events observed in the data after the final selection for the combination of all channels is shown in Table II. The $e\mu$ channel has both the highest signal efficiency and best signal-to-background ratio. There is good agreement between the number of events observed in the data and the various backgrounds in all three channels.

Systematic uncertainties that affect the background estimation and signal efficiencies are listed in Table III. In these estimates, parameters are varied within $\pm 1\sigma$ of the respective theoretical or experimental errors. Sources such as the trigger efficiency, electron and muon identification (ID) efficiencies, jet energy scale (JES), electron and muon momentum resolution, and cross section calculation of Z/γ^*, WW and $t\bar{t}$ events contribute to the systematic uncertainty. The total systematic uncertainties are given in Table III. The uncertainty on the luminosity measurement is 6.5%.

Since after all selection cuts the remaining candidate events are consistent with the background observation, limits on the production cross section times branching ratio $\sigma \times BR(H \to WW^{(*)})$ are derived using a method described in Ref. [15]. This method calculates the cross section limits at 95% C.L. with the integrated luminosity, number of background events, signal acceptance and number of events in data with corresponding errors as inputs. The uncertainty on the background was determined from the statistical and systematic error added in quadrature. Table IV shows the individual upper limits on the cross section times branching ratio for the three different decay channels for six different Higgs boson masses m_H. The different values of the upper limits for the three different channels are related to different background expectations and signal efficiencies. The best limits are achieved for high Higgs masses since background expectations decrease while signal efficiencies increase. A combination of all three channels has been performed by multiplying the individual likelihood functions of all three channels resulting into a combined

TABLE IV: Upper limits at 95% C.L. on the cross section times branching ratio for $\sigma \times BR(H \to WW^{(*)})$ for the combination of all three channels for different Higgs boson masses m_H.

m_H (GeV)	100	120	140	160	180	200
Upper Limits (pb)	20.5	7.6	6.2	5.3	5.7	5.0

likelihood function. This is done separately for all six different masses. The correlation among the three channels given by the luminosity uncertainty and common object ID's is determined to be small. Table IV shows the result of the combination. Figure 5 shows the calculated cross section limits for $\sigma \times BR(H \to WW^{(*)})$ for the different Higgs boson masses compared with predictions from the standard model and alternative scenarios.

To conclude, we have searched for Higgs boson in $H \to WW^{(*)} \to \ell^+\nu\,\ell'^-\bar{\nu}$ $(\ell, \ell' = e, \mu)$ decays in $p\bar{p}$ collisions at $\sqrt{s} = 1.96$ TeV. The data is consistent with expectation from standard model backgrounds. Since no excess has been seen, limits on the production cross section times branching ratio $\sigma \times BR(H \to WW^{(*)})$ have been derived.

We thank the staffs at Fermilab and collaborating institutions, and acknowledge support from the Department of Energy and National Science Foundation (USA), Commissariat à l'Energie Atomique and CNRS/Institut National de Physique Nucléaire et de Physique des Particules (France), Ministry of Education and Science, Agency for Atomic Energy and RF President Grants Program (Russia), CAPES, CNPq, FAPERJ, FAPESP and FUNDUNESP (Brazil), Departments of Atomic Energy and Science and Technology (India), Colciencias (Colombia), CONACyT (Mexico), KRF (Korea), CONICET and UBACyT (Argentina), The Foundation for Fundamental Research on Matter (The Netherlands), PPARC (United Kingdom), Ministry of Education (Czech Republic), Canada Research Chairs Program, CFI, Natural Sciences and Engineering Research Council and WestGrid Project (Canada), BMBF and DFG (Germany), Science Foundation Ireland, A.P. Sloan Foundation, Research Corporation, Texas Advanced Research Program, Alexander von Humboldt Foundation, and the Marie Curie Fellowships.

---

[*] Visitor from University of Zurich, Zurich, Switzerland.

[1] R. Barate *et al.*, Phys. Lett. B **565** (2003) 61.
[2] t. L. E. Group, t. S. Electroweak and H. F. Groups, arXiv:hep-ex/0412015.
[3] A. Djouadi et al., Comput. Phys. Commun. **108**, 56 (1998).
[4] M. Spira, Report DESY T-95-05 (October 1995), arXiv:hep-ph/9510347.
[5] DØ Collaboration, V. Abazov *et al.*, to be submitted to Nucl. Instrum. Methods A; T. LeCompte and H.T. Diehl, Ann. Rev. Nucl. Part. Sci. **50**, 71 (2000).
[6] DØ Collaboration, S. Abachi *et al.*, Nucl. Instrum. Methods Phys. Res. A **338**, 185 (1994).
[7] V. Abramov *et al.*, Nucl. Instrum. Meth. A **419**, 660 (1998).
[8] T. Sjöstrand *et al.*, Comp. Phys. Comm. **135**, 238 (2001).
[9] R. Brun and F. Carminati, CERN Program Library Long Writeup W5013, 1993 (unpublished).
[10] Particle Data Group, S. Eidelman *et al.*, Phys. Lett. B **592**, 1 (2004).
[11] M.L. Mangano *et al.*, J. High Energy Phys. **0307**, 001 (2003).
[12] R. Hamberg, W.L. van Neerven, and T. Matsuura, Nucl. Phys. **B359**, 343 (1991) [Erratum-ibid. **B644**, 403 (2002)].
[13] J. M. Campbell and R. K. Ellis, Phys. Rev. D **60**, 113006 (1999).
[14] N. Kidonakis and R. Vogt, Phys. Rev. D **68**, 114014 (2003).
[15] I. Bertram *et al.*, Fermilab-TM-2104.
[16] E. Arik, M. Arik, S. A. Cetin, T. Conka, A. Mailov and S. Sultansoy, Eur. Phys. J. C **26**, 9 (2002).
[17] M. Carena *et al.*, arXiv:hep-ph/0010338.

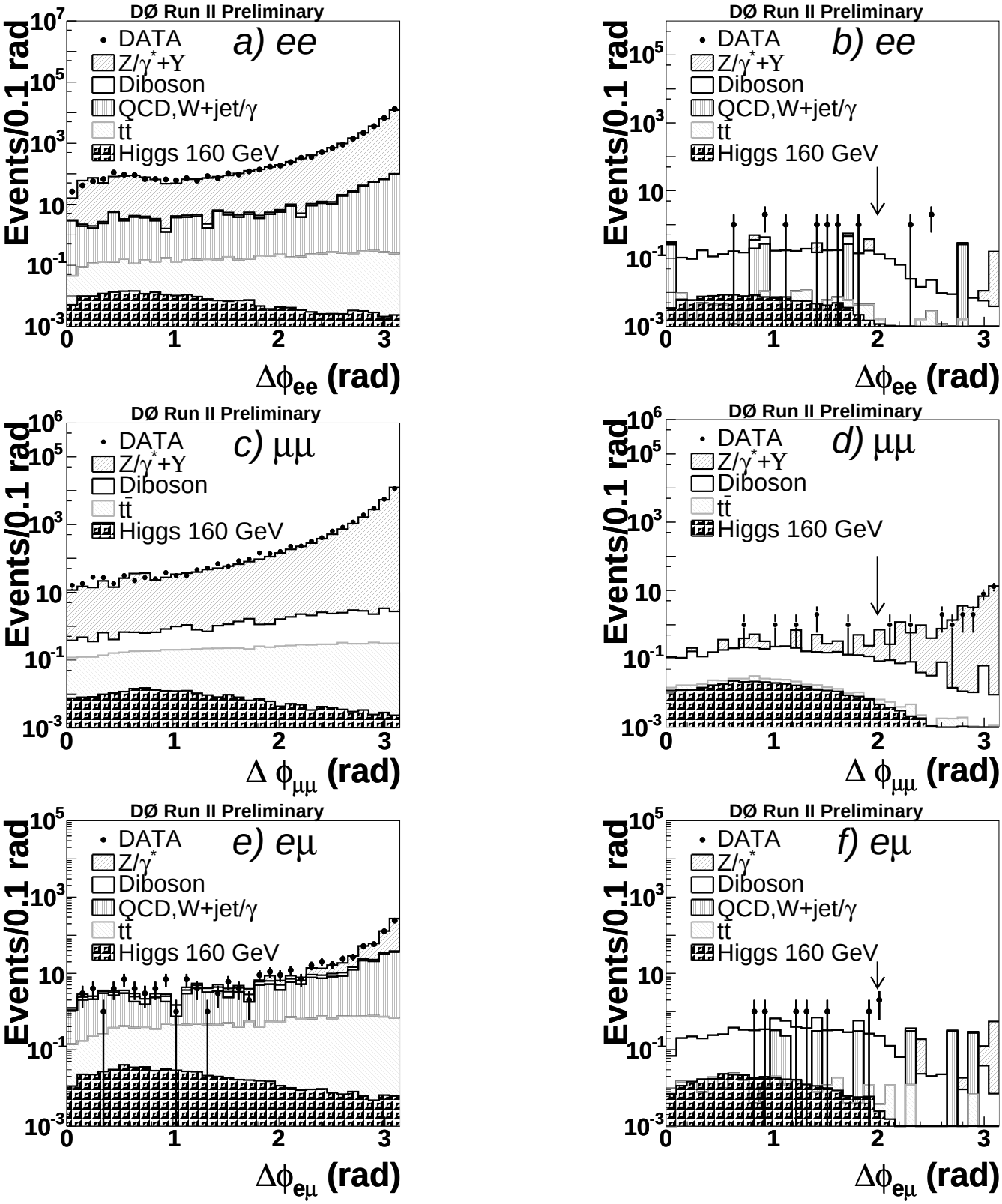

FIG. 1: Distribution of the opening angle $\Delta\phi_{\ell\ell}$ after applying the initial transverse momentum cuts in the (a) ee, (c) $\mu\mu$, and (e) $e\mu$ channel. Figures (b), (d), and (f) show the $\Delta\phi_{\ell\ell}$ distributions after the final selection except for the $\Delta\phi_{\ell\ell}$ criterion for the ee, $\mu\mu$, and $e\mu$ channel, respectively. The arrows indicate the cut values. QCD contribution is negligible in Figs. (c) and (d).

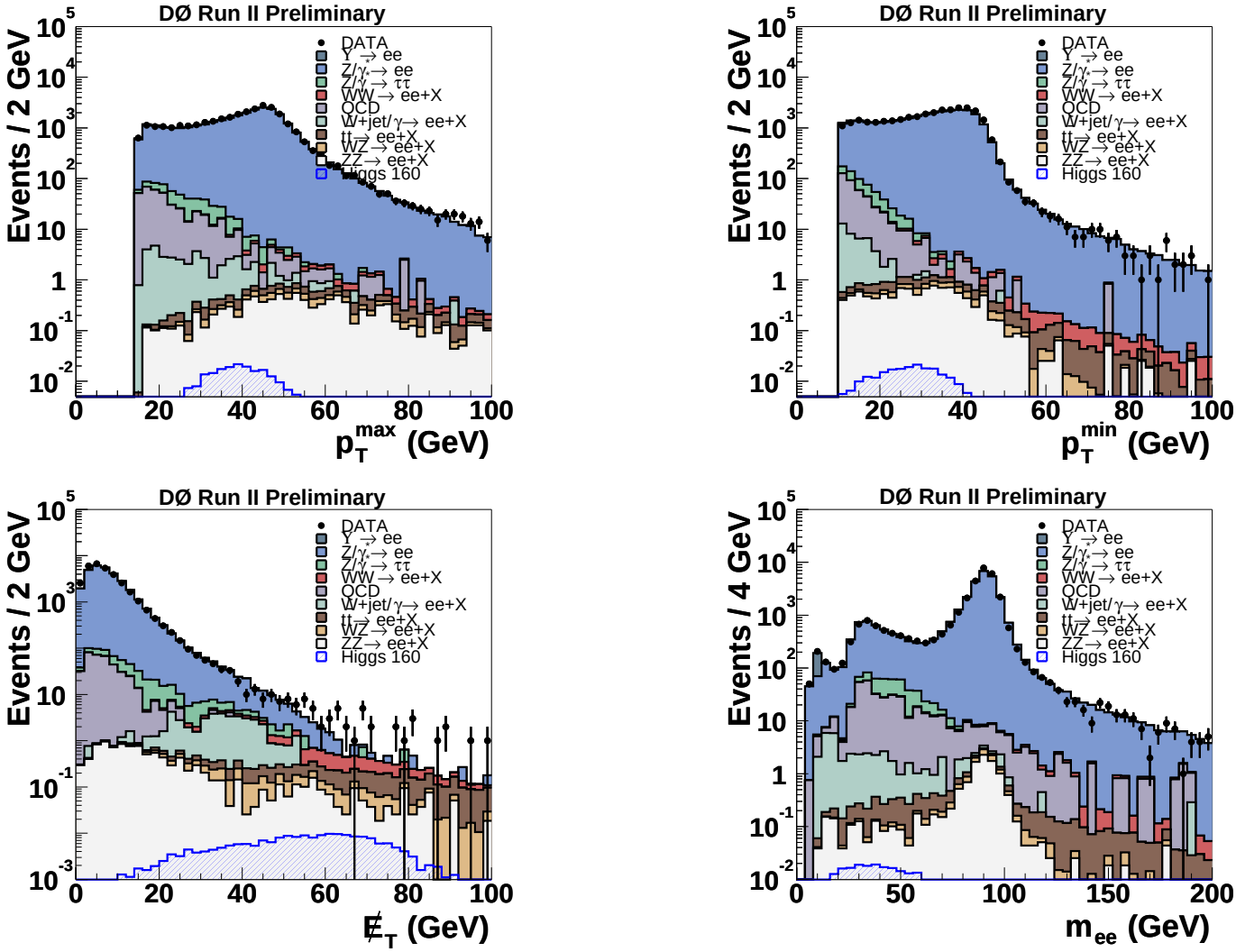

FIG. 2: Distribution of the leading (top left) and trailing electron p_T (top right), missing transverse energy (bottom left), and invariant di-electron mass (bottom right) after applying the initial transverse momentum cuts in the ee channel.

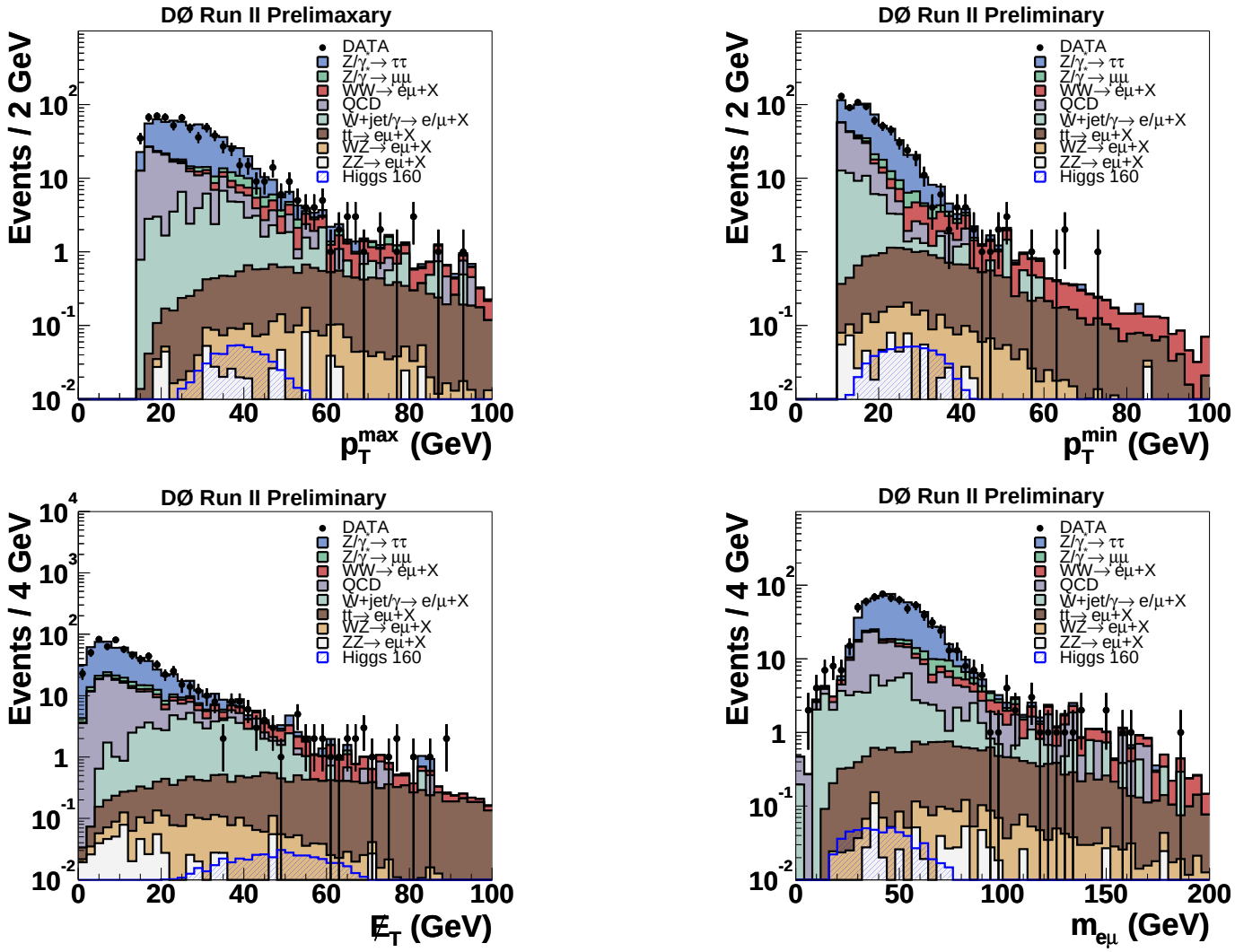

FIG. 3: Distribution of the leading (top left) and trailing lepton p_T (top right), missing transverse energy (bottom left), and invariant di-lepton mass (bottom right) after applying the initial transverse momentum cuts in the $e\mu$ channel.

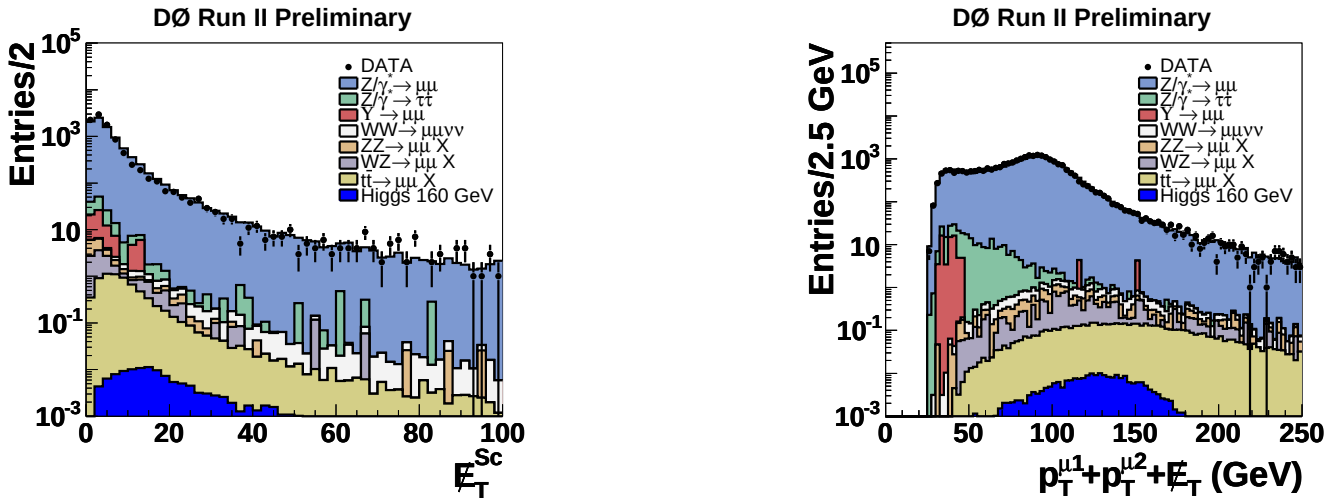

FIG. 4: Distribution of the scaled missing transverse energy $\not\!\!E_T^{\rm Sc}$ (left) and the sum of the leading and trailing muon transverse momentum p_T and the missing transverse energy $\not\!\!E_T$ (right) after applying the initial transverse momentum cuts in the $\mu\mu$ channel.

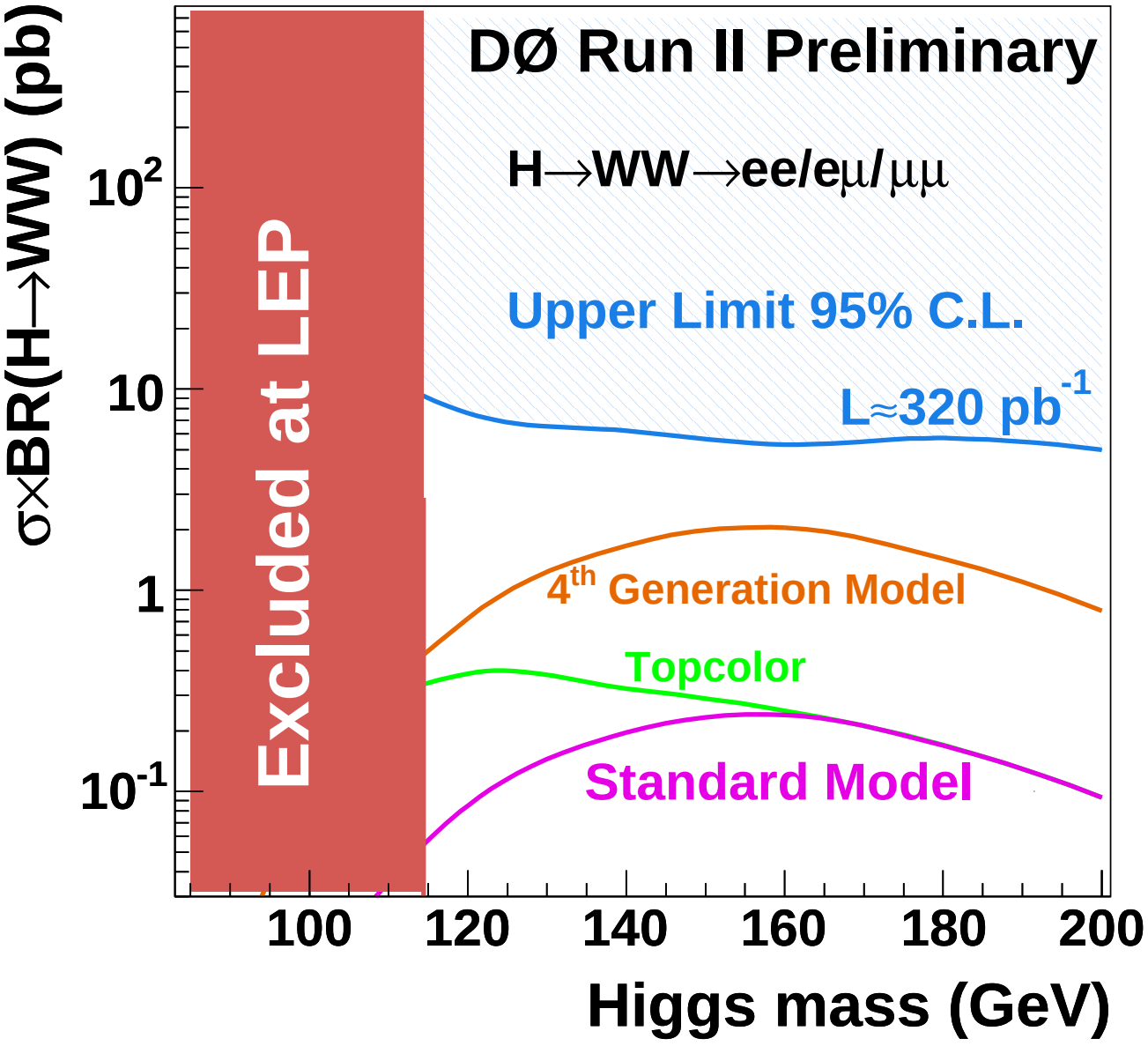

FIG. 5: Excluded cross section times branching ratio $\sigma \times BR(H \to WW^{(*)})$ at 95% C.L. together with expectations from standard model Higgs boson production and alternative models derived using a Bayesian limit calculation. The LEP limit on the standard model Higgs boson production is taken from [1], the 4th generation model is presented in [16], and the topcolor model is presented in [17].